Nonlinear dynamics of vibrating microcantilevers in tapping-mode atomic force microscopy

Kazuyuki Yagasaki*
Department of Mechanical and Systems Engineering, Gifu University, Gifu, Gifu 501-1193, Japan
(Received 2 April 2004; revised manuscript received 30 July 2004; published 15 December 2004)

We consider atomic force microscopy cantilevers tapping on samples and provide theoretical explanations for main findings of numerical computations and experimental measurements by Lee *et al.* [Phys. Rev. B **66**, 115409 (2002)] when the van der Waals force has only a secondary influence on their dynamics. To this end we use the averaging method and an extended version of the subharmonic Melnikov method. Necessary computations for the subharmonic Melnikov method are performed numerically. An analytical framework to describe nonlinear oscillations, including their stability and bifurcations, due to the Derjaguin-Muller-Toporov (DMT) force between the tip and sample surface when operating in tapping mode is given. Our model is basically the same as the previous one of Lee *et al.* although it does not include a parametric excitation term. Numerical computation results are also given to demonstrate our theoretical results.

DOI: 10.1103/PhysRevB.70.245419 PACS number(s): 68.37.Ps, 68.35.Ja, 05.45.−a, 45.10.Hj

I. INTRODUCTION

Atomic force microscopy (AFM) (Refs. 1 and 2) with tapping (or intermittent contact) mode operation[3] has been widely used in nanometer-scale characterization of surfaces, especially for soft materials such as polymers,[3,4] DNA molecules,[5] and proteins.[6] In the standard AFM,[2] a cantilever tip is excited at a frequency close to resonance and the sample is imaged while the forcing amplitude is controlled to keep the oscillation amplitude at a fixed value. In spite of extensive experimental use of the tapping mode, there is still a lack in our understanding of the observed tip motion.

Early studies on the tapping AFM have revealed that interesting "bistable" behavior occurs near the surface and the tip exhibits hysteretic responses when the driving frequency is swept up and down through the primary resonance.[7,8] This phenomenon was explained as a result of an interaction of a harmonic oscillator with attractive and repulsive regions of potential modeled by the van der Waals and Derjaguin-Muller-Toporov (DMT) forces[9–12] or others,[8,13–15] and it causes several artifacts.[16] The nonlinear effects in dynamics of the simple models were investigated mainly through numerical simulations and a few analytical studies based on variants of the multiple scale or averaging method[20,21] have been done.[10,14,15] These analytical techniques are valid only for weakly nonlinear systems and insufficient for the study of the strongly nonlinear tapping mode. Through these researches, the former model, which has the van der Waals and DMT contact forces, is proven to be valid under a wide range of circumstances. Moreover, chaotic tip motions were observed in numerical simulations of a single-degree-of-freedom oscillator model having an impact or hard wall contact with sample surfaces.[17]

More recently, Lee *et al.*[18] performed numerical analysis by a modern computation tool called AUTO,[19] which was developed for numerical continuation and bifurcation analysis of differential equations and is widely used in the community of dynamical systems, although their analysis was limited to the case in which the van der Waals force has only a secondary influence on the cantilever dynamics. Their model, in which the tip-surface interaction is represented by the van der Waals and DMT contact forces, includes not only external excitation but also parametric excitation unlike other similar models.[9–12] Good agreements between their numerical computations and experimental measurements for a freshly cleaved, highly oriented pyrolytic graphite (HOPG) sample were found. In particular, they showed that four types of saddle-node bifurcations, at which a pair of stable and unstable periodic orbits are born in this context, occur in their numerical computations and explained multiple jump phenomena observed in their experiment. Thus, their result also shows that a single-degree-of-freedom oscillator with the van der Waals and DMT contact forces can represent microcantilevers in the tapping mode AFM very precisely.

In this paper we provide theoretical explanations for main findings of numerical computations and experimental measurements in Ref. 18. To this end we use the averaging method[20,21] and an extended version[22] of the subharmonic Melnikov method.[21] The approach of Nony *et al.*[15] for the van der Waals potential also yields a similar result for one of the four saddle-node bifurcations since it occurs in the attractive region of potential. Necessary computations for the subharmonic Melnikov method are performed numerically as in Ref. 23. An analytical framework to describe nonlinear oscillations, including their stability and bifurcations, due to the DMT contact between the tip and sample surface when operating in tapping mode is given. Our model is basically the same as one of Ref. 18 but the parametric excitation term is removed by treating the absolute displacement of the cantilever. Numerical computation results are also given to demonstrate our theoretical results.

The outline of this paper is as follows: In Sec. II our single-degree-of-freedom model is derived from a continuation model of the microcantilever having tip-surface interaction represented by the van der Waals and DMT contact forces. The unperturbed system without the van der Waals, damping and external forcing terms is discussed in Sec. III. Averaging and subharmonic Melnikov analyses are performed in Secs. IV and V, respectively. In Sec. VI numerical computation results by the computer software AUTO (Ref.

 ©2004 The American Physical Society

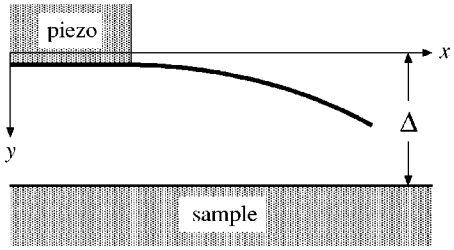

FIG. 1. Cantilever configuration.

19) are provided to be compared with the analytical results of Secs. IV and V. Finally, a summary and some comments are stated in Sec. VII.

II. ANALYTICAL MODEL

Figure 1 shows our analytical model for a microcantilever in tapping mode atomic force microscopy. The base of the beam is excited by a dither piezoelastic actuator with a constant amplitude y_0 and constant frequency Ω so that its displacement is given by $y_0 \cos \Omega t$.

We assume the van der Waals and DMT contact forces between a sphere (tip apex) and a flat surface (sample) in the tip-sample interaction in tapping mode AFM as in Refs. 11 and 18. Let z be the instantaneous tip-sample separation and let a_0 be the intermolecular distance. For $z > a_0$ the tip-sample interaction is given by the van der Waals force

$$F(z) = -\frac{CR}{6z^2}, \tag{1}$$

where C is the Hamaker constant and R is the tip radius. For $z \leqslant a_0$ it is modeled by the DMT contact mechanics[24] as

$$F(z) = -\frac{CR}{6a_0^2} + \frac{4}{3}E_*\sqrt{R}(a_0 - z)^{3/2}, \tag{2}$$

where E_* is the effective elastic modulus of the tip and sample and given by

$$\frac{1}{E_*} = \frac{1-\nu^2}{E} + \frac{1-\nu_s^2}{E_s} \tag{3}$$

with E (resp. E_s) the tip (resp. sample) elastic modulus and ν (resp. ν_s) the tip (resp. sample) Poisson coefficient. The adhesion force in the DMT theory is the resulting van der Waals force at $z = a_0$ so that

$$4\pi R\Gamma = \frac{CR}{6a_0^2}, \tag{4}$$

where Γ is the surface energy. Hence, the equation of motion for the microcantilever becomes

$$\rho A\ddot{v} + D\dot{v} + EIv'''' = -F(\Delta - v(\ell))\,\delta(x-\ell), \tag{5}$$

where ρ, A, and ℓ are, respectively, the mass density, cross section, and length of the beam, and Δ is the tip-sample separation when $F \equiv 0$. The deflection v satisfies the boundary conditions,

$$v(t,0) = y_0 \cos \Omega t,$$

$$v'(t,0) = v''(t,\ell) = v'''(t,\ell) = 0. \tag{6}$$

We approximate the solution of (5) satisfying the boundary conditions (6) as

$$v(t,x) = v_1(t)\psi_1(x) + y_0 \cos \Omega t, \tag{7}$$

where $\psi_1(x)$ is the first mode of the linear problem

$$\rho A\ddot{v} + EIv'''' = 0 \tag{8}$$

under the boundary conditions

$$v(t,0) = v'(t,0) = v''(t,\ell) = v'''(t,\ell) = 0 \tag{9}$$

and given by

$$\psi_1(x) = (\sin \nu_1 x - \sinh \nu_1 x) + \lambda_1(\cos \nu_1 x - \cosh \nu_1 x). \tag{10}$$

Here $\nu_1 \approx 1.8751/\ell$ is the least positive root of

$$\cos \nu_1 \ell \cosh \nu_1 \ell = -1 \tag{11}$$

and

$$\lambda_1 = -\frac{\sinh \nu_1 \ell + \sin \nu_1 \ell}{\cosh \nu_1 \ell + \cos \nu_1 \ell} \approx -1.3622. \tag{12}$$

Substituting (7) into (5) and using the Galerkin method, we obtain

$$\ddot{v}_1 + \delta\omega_1\dot{v}_1 + \omega_1^2 v_1 = -\frac{k_0}{\rho A}F(\Delta - (v_1\psi_1(\ell) + y_0 \cos \Omega t)) + k_1\Omega y_0(\Omega \cos \Omega t + \delta\omega_1 \sin \Omega t), \tag{13}$$

where $\omega_1 = \nu_1^2\sqrt{EI/\rho A}$ is the first mode angular frequency, $\delta = D/\rho A\omega_1$ and

$$k_0 = \psi_1(\ell) \Big/ \int_0^\ell \psi_1^2(x)\mathrm{d}x = \frac{4}{\ell\psi_1(\ell)},$$

$$k_1 = \int_0^\ell \psi_1(x)\mathrm{d}x \Big/ \int_0^\ell \psi_1^2(x)\mathrm{d}x. \tag{14}$$

Let

$$\xi = \frac{1}{\Delta}[v_1(t)\psi_1(\ell) + y_0 \cos \Omega t] \approx \frac{v(t,x)}{\Delta}, \tag{15}$$

and scale the time variable as $t \mapsto \omega_1 t$. Then we can rewrite (13) as

$$\ddot{\xi} + \delta\dot{\xi} + \xi + f(1-\xi) = \gamma(\omega)\cos(\omega t - \theta(\omega)), \tag{16}$$

where

$$f(\zeta) = \frac{4}{\omega_1^2\rho A\Delta\ell}F(\Delta\zeta) = \begin{cases} -\dfrac{\alpha}{\zeta^2} & \text{if } \zeta > a; \\ -\dfrac{\alpha}{a^2} + \beta(a-\zeta)^{3/2} & \text{if } \zeta \leqslant a, \end{cases} \tag{17}$$

TABLE I. Constant values of the cantilever and sample used in our computations.

Quantity	Value
Tip radius	$R=10$ nm
Cantilever cross-section area	$A=8.09\times10^{-11}$ m^2
Cantilever momentum of inertia	$I=3.57\times10^{-23}$ m^4
Cantilever material density	$\rho=2300$ kg/m^3
Cantilever elastic modulus	$E=130$ GPa
Effective elastic modulus	$E_*=10.2$ GPa
First natural frequency	$f_1=44$ kHz
Q factor	$Q=33.3$
Hamaker constant	$C=2.96\times10^{-19}$ J
Intermolecular distance	$a_0=3.8$ Å

$$\gamma(\omega)=\gamma_0\sqrt{(\kappa_1\omega^2+1)^2+(\kappa_1\delta\omega)^2},$$

$$\theta(\omega)=\arctan\left(\frac{\kappa_1\delta\omega}{\kappa_1\omega^2+1}\right)$$

with $a=a_0/\Delta$, $\gamma_0=y_0/\Delta$ and

$$\kappa_1=k_1\psi_1(\ell)-1\approx0.56598,$$

$$\alpha=\frac{2CR}{3\omega_1^2\rho A\Delta^3\ell},\quad \beta=\frac{16E_*\sqrt{\Delta R}}{3\omega_1^2\rho A\ell}. \tag{18}$$

The parameters α and β represent the strength of the attractive and repulsive nonlinear interactions, respectively.

In our computations, we use constant values of the microcantilever and sample in Table I, the data of which come from Ref. 18, and set $\Delta=90$ nm as in that reference. For these values we can estimate $\alpha=7.55\times10^{-7}$, $\beta=4.55\times10^2$, $\delta=0.03$ $(=1/Q)$, and $a=4.22\times10^{-3}$. Henceforth we regard α, δ, and γ_0 as small parameters. Also, note that $\theta(\omega)\approx0$ if $\delta\approx0$. In fact, $\theta(\omega)=0.0108$ for our chosen parameter values when $\omega=1$. Finally, we shift time as $t\mapsto t+\theta(\omega)/\omega$ in (16) to obtain

$$\ddot{\xi}+\delta\dot{\xi}+\xi+f(1-\xi)=\gamma(\omega)\cos\omega t$$

or as a first-order system

$$\dot{\xi}=\eta,\quad \dot{\eta}=-\xi-f(1-\xi)-\delta\eta+\gamma(\omega)\cos\omega t. \tag{19}$$

The techniques used below are applicable only to smooth systems, but Eq. (19) is not smooth. To justify our analyses, we only have to introduce a small interval of length 2μ including the discontinuous point $\xi=1-a$ and take the limit of $\mu\to0$. See also Sec. VI. In the following, we assume this treatment although we do not specifically state it.

III. UNPERTURBED SYSTEM

When the parameters supposed to be small are zero, i.e., $\alpha=\gamma=\delta=0$, Eq. (19) becomes

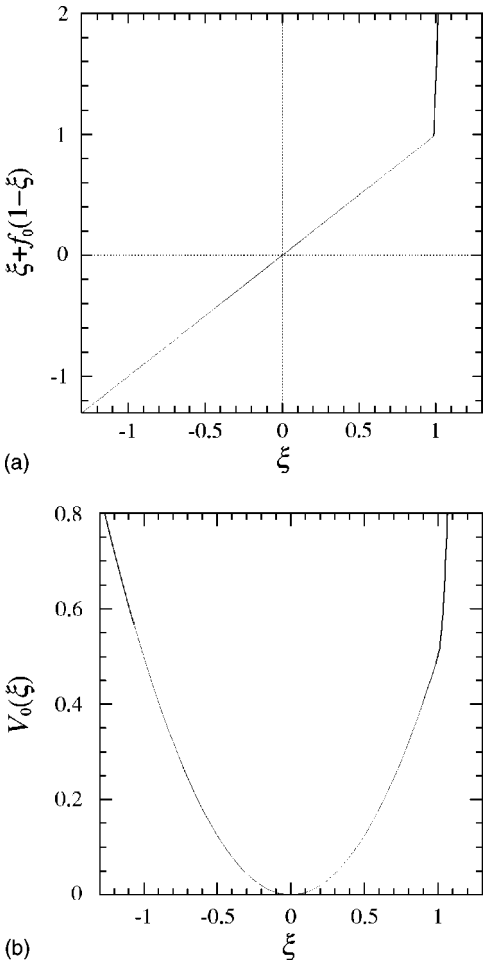

FIG. 2. Restoring force and potential of the unperturbed system (20) for $\beta=4.55\times10^2$ and $a=4.22\times10^{-3}$: (a) Restoring force; (b) potential.

$$\dot{\xi}=\eta,\quad \dot{\eta}=-\xi-f_0(1-\xi), \tag{20}$$

where

$$f_0(\zeta)=\begin{cases}0 & \text{for } \zeta>a;\\ \beta(a-\zeta)^{3/2} & \text{for } \zeta\leqslant a.\end{cases} \tag{21}$$

Note that β is not small although α, δ, $\gamma(\omega)\approx0$. In the following we refer to (20) as the *unperturbed system*. Here we do not mean by this terminology the system without nonlinear force (i.e., $\beta=0$). The unperturbed system (20) is a planar Hamiltonian system with a Hamiltonian function

$$H(\xi,\eta)=V_0(\xi)+\tfrac{1}{2}\eta^2, \tag{22}$$

where $V_0(\xi)$ is the potential given by

$$V_0(\xi)=\frac{1}{2}\xi^2+\int_0^\xi f_0(1-\zeta)\mathrm{d}\zeta. \tag{23}$$

See Figs. 2 and 3 for the restoring force, potential, and phase portrait of (20) with the parameter values. We see that there exist a center at the origin and a family of periodic orbits around it. It is shown in Ref. 25 that more complicated situ-

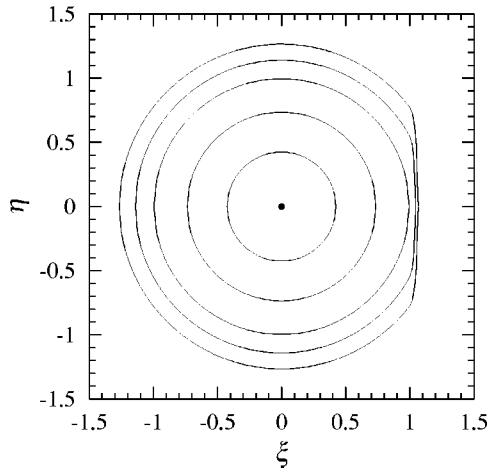

FIG. 3. Phase portrait of the unperturbed system (20) for $\beta=4.55\times10^{2}$ and $a=4.22\times10^{-3}$.

ation occurs when the terms containing α are included, i.e., f_0 is replaced with f, in the unperturbed system.

We parametrize the family of periodic orbits by the Hamiltonian energy $h\geqslant 0$ and represent by $(\overline{\xi}^h(t),\overline{\eta}^h(t))$ the periodic orbit having the Hamiltonian energy h. Denote by T^h the period of $(\overline{\xi}^h(t),\overline{\eta}^h(t))$, and let $(\xi_{\mathrm{L}}^h,0)$ and $(\xi_{\mathrm{R}}^h,0)$ $(\xi_{\mathrm{L}}^h=-\sqrt{2h}<\xi_{\mathrm{R}}^h)$ be two points at which the periodic orbit crosses the ξ-axis in the phase plane (see Fig. 4). Without a loss of generality we can assume that $\overline{\xi}^h(0)=\xi_{\mathrm{L}}^h$ and $\overline{\xi}^h(T^h/2)=\xi_{\mathrm{R}}^h$. From (20) and (22) we have

$$\eta=\frac{\mathrm{d}\xi}{\mathrm{d}t}=\sqrt{2(h-V_0(\xi))} \tag{24}$$

on $(\overline{\xi}^h(t),\overline{\eta}^h(t))$ for $0\leqslant t\leqslant T^h/2$. Rearranging (24) and integrating it yields

$$t=\int_{\xi_{\mathrm{L}}^h}^{\xi}\frac{\mathrm{d}\xi}{\sqrt{2(h-V_0(\xi))}} \tag{25}$$

for $0\leqslant t\leqslant T^h/2$. Hence,

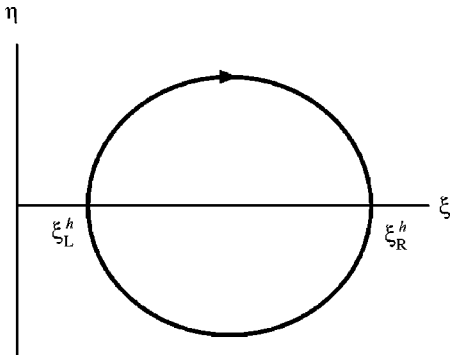

FIG. 4. Definitions of the two points ξ_{L}^h and ξ_{R}^h for a periodic orbit.

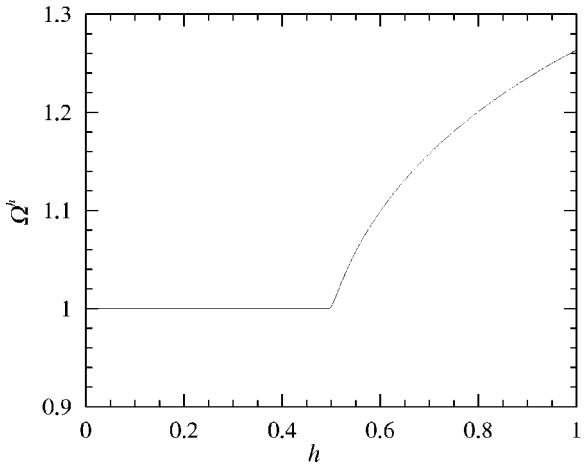

FIG. 5. Dependence of the angular frequency Ω^h on the energy h for $\beta=4.55\times10^{2}$ and $a=4.22\times10^{-3}$.

$$T^h=2\int_{\xi_{\mathrm{L}}^h}^{\xi_{\mathrm{R}}^h}\frac{\mathrm{d}\xi}{\sqrt{2(h-V_0(\xi))}}. \tag{26}$$

We can also compute its angular frequency by $\Omega^h=2\pi/T^h$.

We easily see that if $h\leqslant(1-a)^2/2$, then the periodic orbit $(\overline{\xi}^h(t),\overline{\eta}^h(t))$ is a response of the linear part of (20) so that $T^h=2\pi$ and $\Omega^h=1$. For $h>(1-a)^2/2$ we obtain

$$T^h=2(\pi-\tau^h)+2\int_{1-a}^{\xi_{\mathrm{R}}^h}\frac{\mathrm{d}\xi}{\sqrt{2(h-V_0(\xi))}}, \tag{27}$$

where $\tau^h=\arccos((1-a)/\sqrt{2h})$. The dependence of Ω^h on h is plotted in Fig. 5. Here we used (27) and numerically computed the integral in (27) using the function NINTEGRATE of the computer software MATHEMATICA.[26]

IV. AVERAGING ANALYSES

We return to the forced system (19). Using the averaging method,[20] we describe its dynamics. Introduce a small parameter ϵ such that $0<\epsilon\ll 1$ and set $\alpha=\epsilon\overline{\alpha}$, $\delta=\epsilon\overline{\delta}$, and $\gamma_0=\epsilon\overline{\gamma_0}$. We will choose $\epsilon=1\times10^{-2}$ in our concrete numerical calculations below. Assume that $\omega^2-1=O(\epsilon)$ and set $\epsilon\nu=\omega^2-1$.

A. Case of $\max_t \xi(t)<1-a$

We first consider the case of $\max_t \xi(t)<1-a$. Let

$$\xi=r\cos(\omega t+\phi),\quad \eta=-r\omega\sin(\omega t+\phi). \tag{28}$$

Substituting (28) into (19) and performing the averaging procedure for the resulting equation, we obtain

$$\dot{r}=\frac{\epsilon}{2}[-\overline{\delta}r-\overline{\gamma_0}(\kappa_1+1)\sin\phi],$$

$$r\dot{\phi}=\frac{\epsilon}{2}\left[-\nu r-\frac{\overline{\alpha}r}{(1-r^2)^{3/2}}-\overline{\gamma_0}(\kappa_1+1)\cos\phi\right], \tag{29}$$

where we used the relation $\omega=1+O(\epsilon)$. If the averaged system (29) has a hyperbolic equilibrium, then the original sys-

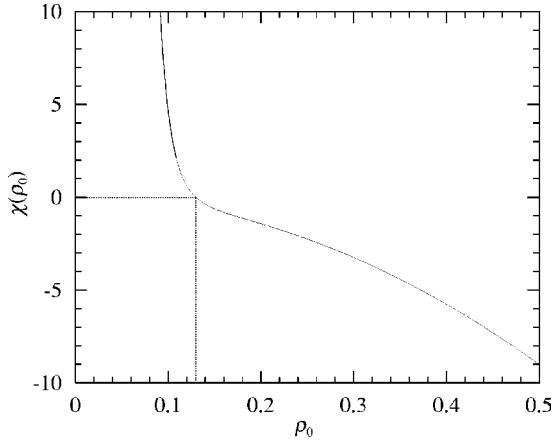

FIG. 6. Graph of $\chi(\rho_0)$ for $\overline{\alpha}=7.55\times10^{-5}$ and $\overline{\delta}=3$.

tem (19) has a hyperbolic periodic orbit near it. Moreover, the periodic orbit in (19) has the same stability type as the corresponding equilibrium in (29).

Let $(r,\phi)=(r_0,\phi_0)$ be an equilibrium in (29). Then

$$-\overline{\delta}r_0-\overline{\gamma}_0(\kappa_1+1)\sin\phi_0=0,$$

$$-\nu r_0-\frac{\overline{\alpha}r_0}{(1-r_0^2)^{3/2}}-\overline{\gamma}_0(\kappa_1+1)\cos\phi_0=0. \tag{30}$$

Eliminating ϕ_0 in (30) and setting $\rho=(1-r_0^2)^{1/2}$, we have

$$(1-\rho^2)\left(\overline{\delta}^2+\nu^2+\frac{2\overline{\alpha}\nu}{\rho^3}+\frac{\overline{\alpha}^2}{\rho^6}\right)=\overline{\gamma}_0^2(\kappa_1+1)^2. \tag{31}$$

Denote the left-hand side of (31) by $g(\rho)$. Differentiating $g(\rho)$ yields

$$\frac{dg}{d\rho}(\rho)=-2\rho\nu^2+\left(\frac{2\overline{\alpha}}{\rho^2}-\frac{6\overline{\alpha}}{\rho^4}\right)\nu+\frac{4\overline{\alpha}^2}{\rho^5}-\frac{6\overline{\alpha}}{\rho^7}-2\overline{\delta}^2\rho. \tag{32}$$

We easily see that if there exists a value of ν such that $g(\rho)$ has a maximum or minimum, say at $\rho=\rho_0$, i.e., $(dg/d\rho)(\rho_0)=0$, then

$$\chi(\rho_0)\equiv\left(\frac{\overline{\alpha}}{\rho_0^2}-\frac{3\overline{\alpha}}{\rho_0^4}\right)^2+2\left(\frac{4\overline{\alpha}^2}{\rho_0^4}-\frac{6\overline{\alpha}^2}{\rho_0^6}-2\overline{\delta}^2\rho_0^2\right)>0. \tag{33}$$

See Fig. 6 for the graph of $\chi(\rho_0)$. Thus, for $\overline{\alpha}=7.55\times10^{-5}$ and $\overline{\delta}=3$, Eq. (33) holds if $\rho_0<\rho_*\approx0.13$. Moreover, there are two values of ν such that $(dg/d\rho)(\rho_0)=0$, which are given by

$$\nu_\pm=-\frac{1}{2\rho_0}\left[-\left(\frac{\overline{\alpha}}{\rho_0^2}-\frac{3\overline{\alpha}}{\rho_0^4}\right)\pm\sqrt{\chi(\rho_0)}\right]. \tag{34}$$

Suppose that $g(\rho)$ has a minimum at $\rho=\rho_0$ and $[\gamma_0(\kappa_1+1)]^2<g(\rho_0)$. Then there exist no root of (31) and no equilibrium of the averaged system (29) such that $r_0\approx\sqrt{1-\rho_0^2}$. If γ_0 is increased so that $[\gamma_0(\kappa_1+1)]^2>g(\rho_0)$, then two equilibria of (29) and hence harmonic orbits of (19)

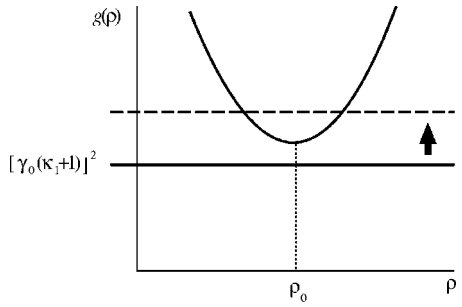

FIG. 7. Creation of two equilibria of the averaged system (29) near a minimum of $g(\rho)$.

with $r\approx\sqrt{1-\rho_0^2}$ are created (see Fig. 7). Similarly, when $g(\rho)$ has a maximum at $\rho=\rho_0$ and $[\gamma_0(\kappa_1+1)]^2>g(\rho_0)$, two harmonic orbits with $r\approx\sqrt{1-\rho_0^2}$ are created if γ_0 is decreased so that $[\gamma_0(\kappa_1+1)]^2<g(\rho_0)$. Thus, we see that a saddle-node bifurcation[21] occurs when $\nu=\nu_\pm$ and $\gamma_0=\sqrt{g(\rho_0)}/(\kappa_1+1)$ for $\sqrt{1-(1-a)^2}<\rho_0<\rho_*$.

The stability of an equilibrium in (29) and hence the associated approximate harmonic orbit in (19) can be determined by the Jacobian matrix of (29) at the equilibrium $(r,\phi)=(r_0,\phi_0)$,

$$\frac{\epsilon}{2}\begin{pmatrix}-\overline{\delta} & -\overline{\gamma}\cos\phi_0\\ -\dfrac{3\overline{\alpha}r_0}{(1-r_0^2)^{5/2}}+\dfrac{\overline{\gamma}}{r_0^2}\cos\phi_0 & \dfrac{\overline{\gamma}}{r_0}\sin\phi_0\end{pmatrix}, \tag{35}$$

where $\overline{\gamma}=\overline{\gamma}_0(\kappa_1+1)$. The equilibrium and harmonic orbit are stable (resp. unstable) if the matrix (35) has only eigenvalues with negative real parts (resp. an eigenvalue with a positive real part).[21] When one of the eigenvalues has the null real part, their stability is critical and a saddle-node bifurcation occurs if special restriction or symmetry does not exist as in our situation. After a simple calculation, we easily see that it is stable (resp. unstable) if $(dg/d\rho)(\rho)<0$ [resp. $(dg/d\rho)(\rho)>0$].

B. Case of $\max_t \xi(t)>1-a$

We next consider the case of $\max_t \xi(t)>1-a$. We assume that $\max_t \xi(t)\approx1-a$ and set $r=1-a+\epsilon^{1/2}u$ in (28). Note that $\xi=(1-a+\epsilon^{1/2}u)\cos(\omega t+\phi)>1-a$ when $\omega t+\phi\in[-\phi_\epsilon,\phi_\epsilon]$, where

$$\phi_\epsilon=\arccos\left(\frac{1-a}{1-a+\epsilon^{1/2}u}\right)=\epsilon^{1/4}\sqrt{\frac{2u}{1-a}}+O(\epsilon^{3/4}). \tag{36}$$

Substituting (28) into (19) and performing the averaging procedure for the resulting equation, we obtain

$$\dot{u}=\tfrac{1}{2}[-\overline{\delta}(1-a)-\overline{\gamma}_0(\kappa_1+1)\sin\phi],$$

$$\dot{\phi} = \frac{\epsilon}{2}\left[-\nu - \frac{\overline{\alpha}}{(a(2-a))^{3/2}} + \frac{2\sqrt{2}}{\pi(1-a)^{3/2}}\beta u^2 - \frac{\overline{\gamma_0}(\kappa_1+1)}{1-a}\cos\phi \right]. \tag{37}$$

Here we note that by (36)

$$\frac{1}{2\pi}\int_{-\phi_\epsilon}^{\phi_\epsilon} (\epsilon^{1/2}u\cos\phi)^{3/2}\cos\phi \mathrm{d}\phi = \frac{\epsilon}{\pi}\sqrt{\frac{2}{1-a}}u^2 + O(\epsilon^{3/2}) \tag{38}$$

since $\cos\phi = 1 + O(\phi^2)$ when ϕ is small.

Let $(u,\phi) = (u_0,\phi_0)$ be an equilibrium in (37). Then

$$-\overline{\delta}(1-a) - \overline{\gamma_0}(\kappa_1+1)\sin\phi_0 = 0,$$

$$-\nu - \frac{\overline{\alpha}}{(a(2-a))^{3/2}} + \frac{2\sqrt{2}}{\pi(1-a)^{3/2}}\beta u_0^2 - \frac{\overline{\gamma_0}(\kappa_1+1)}{1-a}\cos\phi_0 = 0. \tag{39}$$

From the first equation of (39) we obtain $\phi_0 = -\phi_*$ or $-\pi + \phi_*$, where

$$\phi_* = \arcsin\left(\frac{\overline{\delta}(1-a)}{\overline{\gamma_0}(\kappa_1+1)}\right) \tag{40}$$

with the range of arcsin chosen as $[-\pi/2, \pi/2]$. Using the second equation of (39) and (40), we have

$$u_0^2 - \frac{\pi(1-a)^{3/2}}{2\sqrt{2}\beta}\left(\nu + \frac{\overline{\alpha}}{(a(2-a))^{3/2}} \pm \sqrt{\left(\frac{\overline{\gamma_0}(\kappa_1+1)}{1-a}\right)^2 - \overline{\delta}^2}\right) = 0, \tag{41}$$

where the upper or lower sign is chosen depending on whether $\phi_0 = -\phi_*$ or $\phi_0 = -\pi + \phi_*$. Hence, if

$$\nu > -\frac{\overline{\alpha}}{(a(2-a))^{3/2}} \mp \sqrt{\left(\frac{\overline{\gamma_0}(\kappa_1+1)}{1-a}\right)^2 - \overline{\delta}^2}, \tag{42}$$

then there are two equilibria in (37). Moreover, if

$$\nu = -\frac{\overline{\alpha}}{(a(2-a))^{3/2}} \mp \sqrt{\left(\frac{\overline{\gamma_0}(\kappa_1+1)}{1-a}\right)^2 - \overline{\delta}^2}, \tag{43}$$

then two equilibria appear, i.e., a saddle-node bifurcation occurs. The stability of the equilibrium can be determined by the Jacobian matrix of (37). Thus, we show that they are stable (resp. unstable) if $u_0\cos\phi_0 > 0$ (resp. < 0).

The equilibria with $u_0 > 0$ in (37) correspond to approximate harmonic orbits in (19). However, we cannot immediately obtain a similar statement for the equilibria with $u_0 \leqslant 0$ in (37). An approach to treat this problem precisely is to use the approach stated at the end of Sec. II and perform a higher-order approximation. Fortunately, we can obtain almost the same statement without such a troublesome treatment as follows.

From the above analyses of this section we conclude that, for $\epsilon > 0$ sufficiently small, a pair of harmonic orbits having different stability, exist in (19) if condition (42) holds. One of them satisfies $\max_t \xi(t) < 1-a$ and the other $\max_t \xi(t) > 1-a$. Such a pair of harmonic orbits do not exist if the opposite inequality holds in (42). Hence, a saddle-node bifurcation of harmonic orbits in (19) occurs near the parameter values satisfying (43).

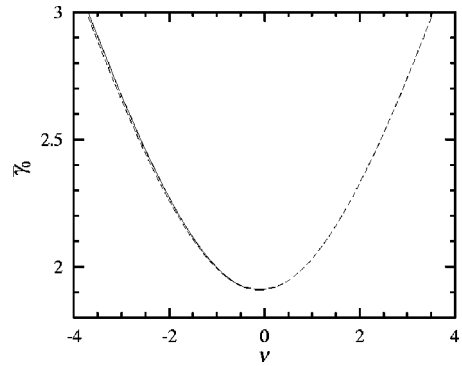

FIG. 8. Approximate saddle-node bifurcation curves for the forced system (19) in the $(\nu, \overline{\gamma_0})$-plane for $\overline{\alpha} = 7.55\times10^{-5}$, $\overline{\delta} = 3$, $\beta = 4.55\times10^2$, and $a = 4.22\times10^{-3}$. The solid and dashed curves represent the analytical results obtained by the analyses of Secs. IV A and IV B, respectively.

In Fig. 8 we show two approximate saddle-node bifurcation curves obtained by the analyses of Secs. IV A and IV B in the $(\nu, \overline{\gamma_0})$-plane. The results of Secs. IV A and IV B are plotted as solid and dashed curves, respectively, although they are very close each other in the region of $\nu < 0$. These saddle-node bifurcations correspond to three of four types of saddle-node bifurcations observed near the primary resonance by Lee *et al.*:[18] Noncontact harmonic orbits are born at the first type denoted by "SN2" in Ref. 18, and tapping harmonic orbits are born at the second and third types denoted by "SN1" and "SN4," respectively, in Ref. 18. The remainder one denoted by "SN3" in Ref. 18 and observed relatively away from the primary resonance is detected by a different method in the next section.

Figure 9 shows the dependence on the detuning parameter ν of r_0 and ϕ_0 for $\epsilon = 0.01$ and $\overline{\gamma_0} = 2.09$, which corresponds to $y_0 \approx 1.9$ nm in the main experimental and numerical example of Lee *et al.*[18] Here we set $r_0 = 1 - a + \epsilon^{1/2}u_0$ for the result of Sec. IV B. See also Figs. 10 and 11.

V. SUBHARMONIC MELNIKOV ANALYSIS

We next analyze harmonic orbits in the forced system (19) when $\max_t \xi(t) > 1-a$, without assuming that $\max_t \xi(t) \approx 1-a$ and $\omega \approx 1$. Our approach used here is an extended version[22] of the subharmonic Melnikov method.[21] Using the extended method, we can easily analyze the stability of periodic orbits and their Hopf bifurcations as well as their existence and saddle-node bifurcations. See Ref. 22 for the proofs and details of this method.

As in Sec. IV, we set $\alpha = \epsilon\overline{\alpha}$, $\delta = \epsilon\overline{\delta}$, and $\gamma_0 = \epsilon\overline{\gamma_0}$, where $0 < \epsilon \ll 1$. We compute the $1/1$th subharmonic Melnikov functions, $M^h(t_0)$ and $L^h(t_0)$, for the unperturbed periodic orbit $(\overline{\xi}^h(t), \overline{\eta}^h(t))$ as

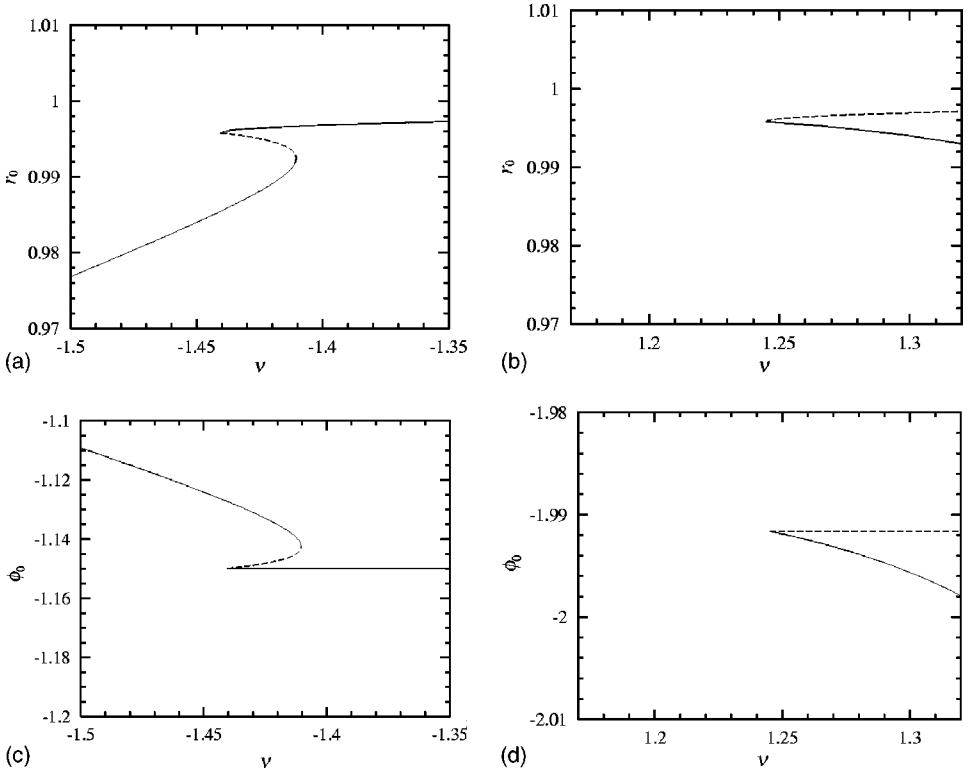

FIG. 9. Dependence of the approximate harmonic orbit on the detuning parameter ν for $\overline{\gamma_0}=2.09$ when $\epsilon=0.01$, $\overline{\alpha}=7.55\times10^{-5}$, $\beta=4.55\times10^{2}$, $\overline{\delta}=3$, and $a=4.22\times10^{-3}$: (a) and (b) amplitude r_0; (c) and (d) phase ϕ_0. The solid and dashed curves represent stable and unstable orbits, respectively.

$$M^h(t_0)=\int_0^{T^h}\overline{\eta}^h(t)[-\overline{\delta}\overline{\eta}^h(t)+\overline{\gamma}(\omega)\cos\,\omega(t+t_0)]\mathrm{d}t$$

$$=-\overline{\gamma}(\omega)A(h)\sin\,\omega t_0-\overline{\delta}B(h),$$

$$L^h(t_0)=-\overline{\delta}T^h<0, \tag{44}$$

where $\overline{\gamma}(\omega)=(\kappa_1\omega^2+1)\overline{\gamma_0}$, the primary resonance condition $T^h=2\pi/\omega$ holds and

$$A(h)=\int_0^{T^h}\overline{\eta}^h(t)\sin\,\omega t\mathrm{d}t,$$

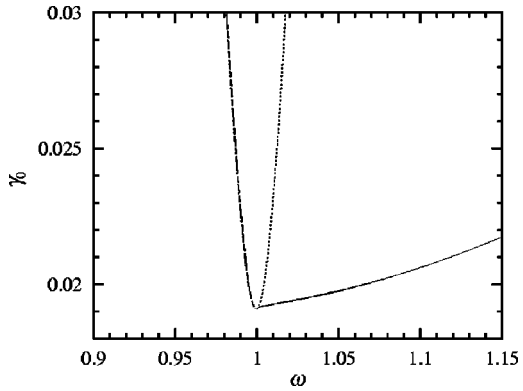

FIG. 10. Approximate saddle-node bifurcation curves for the forced system (19) in the (ω,γ_0)-plane for $\alpha=7.55\times10^{-7}$, $\beta=4.55\times10^{2}$, $\delta=0.03$, and $a=4.22\times10^{-3}$.

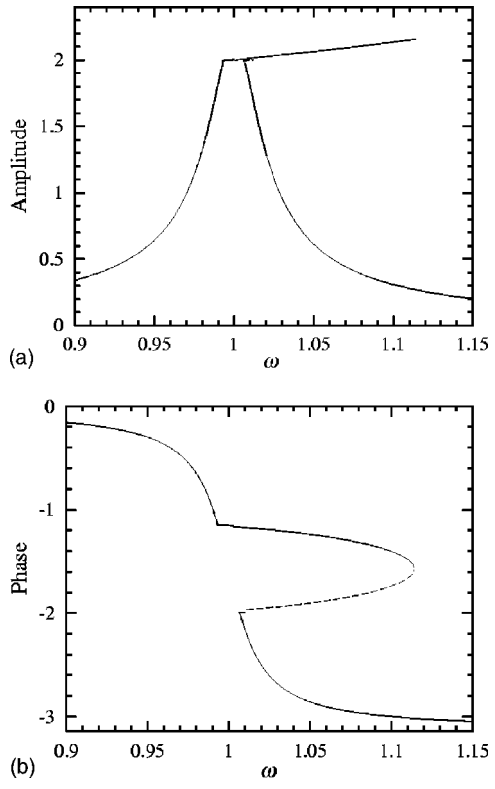

FIG. 11. Dependence of the approximate harmonic orbit on the angular frequency ω for $\gamma_0=0.0209$ when $\alpha=7.55\times10^{-7}$, $\beta=4.55\times10^{2}$, $\delta=0.03$, and $a=4.22\times10^{-3}$: (a) Peak-to-peak amplitude; (b) phase ϕ_0. The solid and dashed curves represent stable and unstable orbits, respectively.

$$B(h) = \int_0^{T^h} [\overline{\eta}^h(t)]^2 \mathrm{d}t. \tag{45}$$

Here we used the fact that $\overline{\eta}^h(t)$ is an odd function of t. Noting that

$$\overline{\eta}^h(t) = \sqrt{2h}\sin t \tag{46}$$

for $0 \leqslant t \leqslant \pi - \tau^h$ and utilizing the relations (24) and (25), we obtain

$$\begin{aligned} A(h) = &-\frac{2\sqrt{2h}}{\omega^2-1}[\omega \sin\tau^h \cos\omega(\pi-\tau^h) \\ &+ \cos\tau^h \sin\omega(\pi-\tau^h)] \\ &+ 2\int_{1-a}^{\xi_R^h} \sin\left(\Omega^h\left[\int_{1-a}^{\xi_1} \frac{\mathrm{d}\xi}{\sqrt{2(h-V_0(\xi))}} + \pi - \tau^h\right]\right)\mathrm{d}\xi_1, \end{aligned}$$

$$B(h) = h[2(\pi-\tau^h) + \sin 2\tau^h] + 2\int_{1-a}^{\xi_R^h} \sqrt{2(h-V_0(\xi))}\,\mathrm{d}\xi. \tag{47}$$

It is easy to numerically compute $A(h)$ and $B(h)$ like the period of the unperturbed periodic orbits, T^h, in (27).

Noting that $\mathrm{d}\Omega^h/\mathrm{d}h > 0$ (see Fig. 5) and applying the extended theory of Ref. 22, we can prove the following results:

(i) If

$$\frac{\overline{\gamma_0}}{\overline{\delta}} > \frac{B(h)}{(\kappa_1\omega^2+1)|A(h)|}, \tag{48}$$

then $M^h(t_0)$ has two simple zeros, $t=\overline{t_0}$ and $\pi/\omega - \overline{t_0}$, and there are two harmonic orbits $(\xi_1(t), \eta_1(t))$ and $(\xi_2(t), \eta_2(t))$, which exist near $(\xi^h(t-\overline{t_0}), \overline{\eta}^h(t-\overline{t_0}))$ and $(\xi^h(t+\pi/\omega+\overline{t_0}), \overline{\eta}^h(t+\pi/\omega+\overline{t_0}))$, respectively, where $-\pi/2 \leqslant \omega\overline{t_0} \leqslant \pi/2$ and

$$\overline{t_0} = -\frac{1}{\omega}\arcsin\left(\frac{\overline{\delta}B(h)}{\overline{\gamma}(\omega)A(h)}\right) \tag{49}$$

(see Theorem 3.1 of Ref. 22). Thus, the phase of these harmonic orbits can be approximately estimated as $\phi_0 = \omega\overline{t_0}$ or $-\pi - \omega\overline{t_0}$.

(ii) The harmonic orbit $(\xi_1(t), \eta_1(t))$ is stable (resp. unstable) and $(\xi_2(t), \eta_2(t))$ is unstable (resp. stable) if $A(h) < 0$ [resp. $A(h) > 0$].[27]

(iii) Near

$$\frac{\overline{\gamma_0}}{\overline{\delta}} = \frac{B(h)}{(\kappa_1\omega^2+1)|A(h)|}, \tag{50}$$

in the parameter space, a saddle-node bifurcation occurs and the periodic orbits $(\xi_j(t), \eta_j(t))$, $j=1,2$, are born (see Theorem 4.1 of Ref. 22).

Figure 10 shows the approximate saddle-node bifurcation curves obtained in the previous and present sections, in the (ω, γ_0)-plane. The result of Sec. V is plotted as a solid curve while ones of Secs. IV A and IV B are plotted as dashed and dotted curves, respectively. Note that the dashed and dotted curves are very close to each other in the region of $\omega < 1$.

In Fig. 11 we show the dependence on the angular frequency ω of the peak-to-peak amplitude and phase ϕ_0 for the approximate harmonic orbits, along with their stability, for $\gamma_0 = 0.0209$, which corresponds to $y_0 \approx 1.9$ nm and was chosen in the main experimental and numerical examples of Lee *et al.*[18] Here the peak-to-peak amplitude is estimated as $2r_0$, $2(1-a-\epsilon^{1/2}u_0)$ and $\xi_R^h - \xi_L^h$ for the analyses of Secs. IV A, IV B, and V, respectively, where h is given as a root of $\Omega^h = \omega$. We see that our theory not only qualitatively but also quantitatively explains their numerical and experimental results very well [cf. Figs. 2(c) and 2(d), and Fig. 10 of Ref. 18].

VI. NUMERICAL CONTINUATION AND BIFURCATION ANALYSES

We demonstrate the above theoretical results by numerical continuation and bifurcation analyses by AUTO.[19] A computation similar to those given in Ref. 18 was first performed. In the computation, to avoid complicated treatments due to its nonsmoothness at $\zeta = a$ [see Eq. (17)], the function f was replaced by

$$f_\mu(\zeta) = \begin{cases} -\dfrac{\alpha}{\zeta^2} & \text{if } \zeta > a+\mu; \\ -\dfrac{\alpha}{a^2} + \beta(a-\zeta)^{3/2} & \text{if } \zeta \leqslant a-\mu; \\ -\dfrac{\alpha}{\zeta^2} + k_3(\zeta-a-\mu)^3 + k_2(\zeta-a-\mu)^2 & \text{otherwise,} \end{cases} \tag{51}$$

where μ is a small value and

$$k_2 = \frac{\alpha(3\mu^2 - 9a\mu + 2a^2)}{4a^2(a-\mu)^3\mu},$$

$$\begin{aligned} k_3 = \frac{1}{8a^2(a-\mu)^3\mu^{3/2}}[&a^2\beta\mu^3 - 3a^3\beta\mu^2 + 2\alpha\mu^{3/2} + 3a^4\beta\mu \\ &- 6a\alpha\mu^{1/2} - a^5\beta]. \end{aligned} \tag{52}$$

We have $f(\zeta) = f_\mu(\zeta)$ except the small interval $(a-\mu, a+\mu)$ and $f(\zeta) = f_\mu(\zeta)$ and $f'(\zeta) = f'_\mu(\zeta)$ at $\zeta = a \pm \mu$. We set $\mu = 1 \times 10^{-5}$ in our computations.

Figure 12 shows the dependence on the angular frequency ω of the peak-to-peak amplitude for the numerically computed harmonic orbits, along with their stability, for $\gamma_0 = 0.0209$. We find a fairly good agreement between the theoretical result of Fig. 11(a) and numerical result of Fig. 12. On the other hand, we could not succeed in continuation of the saddle-node bifurcations by AUTO except for noncontact harmonic orbits. To compute other saddle-node bifurcation curves numerically, the following boundary value problem was treated.

Denote $\xi = \xi_1$ and $\eta = \eta_1$ for $\xi < 1-a$ and $\xi = \xi_2$ and $\eta = \eta_2$ for $\xi > 1-a$. Let $t = T_0$ be the time when $\xi(t)$ crosses

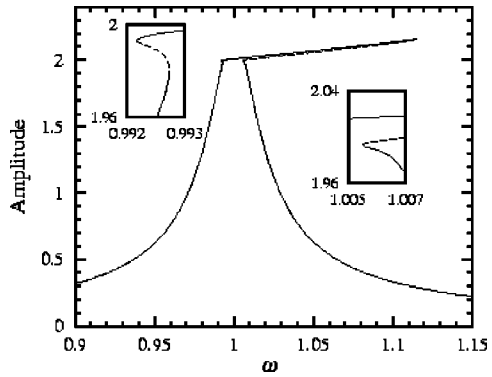

FIG. 12. Numerically computed peak-to-peak amplitude for the forced system (19) when $\gamma_0=0.0209$, $\delta=0.03$, $\alpha=7.55\times10^{-7}$, $\beta=4.55\times10^{2}$, and $a=4.22\times10^{-3}$. Here the function f was replaced by f_μ in (51) with $\mu=1\times10^{-5}$.

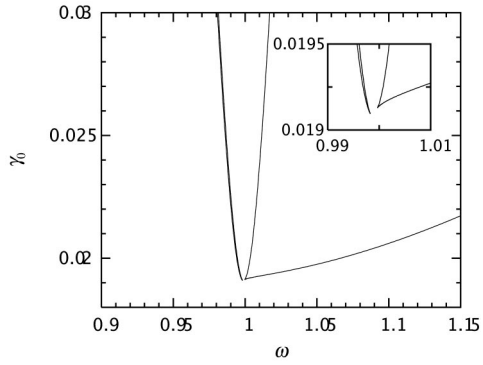

FIG. 13. Numerically computed saddle-node bifurcation curves for the forced system (19) in the (ω,γ_0)-plane for $\alpha=7.55\times10^{-7}$, $\beta=4.55\times10^{2}$, $\delta=0.03$, and $a=4.22\times10^{-3}$.

the axis $\xi=1-a$ from the above [i.e., $\eta(T_0)<0$] and let $t=T_0+T_1$ be the time when $\xi(t)$ crosses the axis $\xi=1-a$ from the below [i.e., $\eta(T_0+T_1)>0$]. In addition, assume that ξ does not cross the axis $\xi=1-a$ at other times, and shift the time for (ξ_1,η_1) and (ξ_2,η_2) such that

$$\xi_1(0)=\xi_1(T_1)=\xi_2(0)=1-a,$$

$$\eta_1(T_1)=\eta_2(0)>0. \tag{53}$$

We have

$$\dot{\xi}_1=\eta_1,$$

$$\dot{\eta}_1=-\xi_1+\frac{\alpha}{(1-\xi_1)^2}-\delta\eta_1+\gamma(\omega)\cos\omega(t+T_0) \tag{54}$$

and

$$\dot{\xi}_2=\eta_2,$$

$$\dot{\eta}_2=-\xi_2+\frac{\alpha}{a^2}-\beta(a-1+\xi_2)^{3/2}-\delta\eta_2+\gamma(\omega)\cos\omega(t+T_0+T_1). \tag{55}$$

For a harmonic orbit of (19) we have

$$\xi_1(0)=\xi_2(T-T_1),\quad \eta_1(0)=\eta_2(T-T_1), \tag{56}$$

where $T=2\pi/\omega$. Thus, we can reduce the problem of computing a harmonic orbit of the forced system (19) to the boundary value problem for (54) and (55) under the boundary conditions (53) and (56).

Define the Poincaré map[21] $P:\mathbb{R}^2\to\mathbb{R}^2$ as

$$(\xi_1(0),\eta_1(0))\mapsto(\xi_2(T-T_1),\eta_2(T-T_1)), \tag{57}$$

where $(\xi_1(t),\eta_1(t))$ and $(\xi_2(t),\eta_2(t))$ are, respectively, solutions of (54) and (55) satisfying (53). Let $\Phi_1(t)$ and $\Phi_2(t)$ be the fundamental matrices of the variational equations about the solutions of (54) and (55), such that $\Phi_1(0)$ and $\Phi_2(0)$ are the 2×2 identity matrix. Then the Jacobian matrix of the Poincaré map can be computed as

$$DP=\Phi_2(T-T_1)\Phi_1(T_1). \tag{58}$$

If DP has a unit eigenvalue for some parameter values, then a saddle-node bifurcation occurs at the parameter values.[21] Hence, to obtain a saddle-node bifurcation curve, we only have to continue the parameter values such that DP has a unit eigenvalue. Such a computation can also be performed easily by AUTO.

Figure 13 shows saddle-node bifurcation curves numerically computed by this approach, along with one obtained by a numerical continuation of saddle-node bifurcations for noncontact harmonic orbits in (19) with $f=f_\mu$. In Fig. 13, for the left and right branches of saddle-node bifurcations, we observe cusp bifurcations,[21] at which two saddle-node bifurcation curves meet.

An excellent agreement between the theoretical result of Fig. 10 and numerical result of Fig. 13 is found except the cusp bifurcation. To treat the cusp bifurcations analytically, we need a sophisticated analysis as in Refs. 22 and 28.

VII. CONCLUDING REMARKS

We have theoretically explained main findings of numerical computations and experimental measurements by Lee *et al.*[18] The analytical tools used here were the averaging method[20,21] and an extended version[22] of the subharmonic Melnikov method.[21] In our numerical computations by the computer software AUTO,[19] we also reproduced the main numerical results of Ref. 18 and, furthermore, succeeded in continuation of saddle-node bifurcations by treating a nonlinear boundary value problem. A fairly good agreement between the analytical and numerical results was found. Our results indicate that numerical and experimental observations by Lee *et al.*[18] will be still valid for much wider parameter regions.

Here we only considered the same situation as Lee *et al.*,[18] so that the tip-sample separation was $\Delta=90$ nm and relatively large. Consequently, the influence of the van der Waals force on the dynamics of the microcantilever was so small that we could treat it as a small perturbation in the equation of motion. In the practical operating regime of tapping mode AFM the tip-sample separation is further small.

Hence, we expect the performance of the tapping mode AFM can be improved by using a regime in which the van der Waals force is a primary influence on the dynamics of microcantilevers. Detailed analyses for bifurcations and chaos in such a regime are desired and given elsewhere.[25]

As we have seen here, "nonlinearity" is essential in understanding the dynamics of microcantilevers in tapping mode AFM. It is plausible that "nonlinearity" plays an important role in other aspects of nanotechnology. So better understandings of such nonlinear phenomena will be helpful and desirable for further progress of this attractive and exciting field. Dynamical systems theory[21] must also be useful in this context.

ACKNOWLEDGMENTS

The author thanks Dr. Hirohisa Tamagawa for helpful discussions and Dr. Petri Piiroinen for useful advice on drawing Fig. 13.

*Electronic address: yagasaki@cc.gifu-u.ac.jp

[1] G. Binnig, C.F. Quate, and Ch. Gerber, Phys. Rev. Lett. **56**, 930 (1986); D. Rugar and P. Hansma, Phys. Today **43** (10), 23 (1990); G. Binnig and H. Rohrer, Rev. Mod. Phys. **71**, S324 (1999).

[2] T.R. Albrecht, P. Grütter, D. Horne, and D. Rugar, J. Appl. Phys. **69**, 668 (1991).

[3] Q. Zhong, D. Inniss, K. Kjoller, and V.B. Elings, Surf. Sci. Lett. **290**, L688 (1993).

[4] W. Stoker, J. Bechmann, R. Stadler, and J.P. Rabe, Macromolecules **29**, 502 (1996); S.N. Magonov, V. Elings, and M.-H. Whangbo, Surf. Sci. **375**, L385 (1997); S.N. Magonov, V. Elings, and V.S. Papkov, Polymer **38**, 297 (1997); S.N. Magonov, J. Cleveland, V. Elings, D. Denley, and M.-H. Whangbo, Surf. Sci. **389**, 201 (1997); G. Bar, Y. Thomann, and M.-H. Whangbo, Langmuir **14**, 1219 (1998); G. Haugstad and R.R. Jones, Ultramicroscopy **76**, 77 (1999).

[5] P. Hansma, J.P. Cleveland, M. Radmacher, D.A. Walters, P.E. Hillner, M. Bezanilla, M. Fritz, D. Vie, H.G. Hansma, C.B. Prater, J. Massie, L. Fukunaga, J. Gurley, and V. Elings, Appl. Phys. Lett. **64**, 1738 (1994); E. Margeat, C. Le Grimellec, and C.A. Royer, Biophys. J. **75**, 2712 (1999).

[6] C. Möller, M. Allen, V. Elings, A. Engel, and D. Müller, Biophys. J. **77**, 1150 (1999); A. San Paulo and R. García, *ibid.* **78**, 1599 (2000).

[7] P. Gleyzes, P.K. Kuo, and A.C. Boccara, Appl. Phys. Lett. **58**, 2989 (1991).

[8] A. Kühle, A.H. Sørensen, and J. Bohr, J. Appl. Phys. **81**, 652 (1997).

[9] J. Tamayo and R. García, Langmuir **12**, 4430 (1996); M. Marth, D. Maier, J. Honerkamp, R. Brandsch, and G. Bar, J. Appl. Phys. **85**, 7030 (1999).

[10] L. Wang, Appl. Phys. Lett. **73**, 3781 (1998).

[11] R. García and A. San Paulo, Phys. Rev. B **60**, 4961 (1999).

[12] R. García and A. San Paulo, Phys. Rev. B **61**, R13 381 (2000).

[13] B. Anczykowski, D. Krüger, and H. Fuchs, Phys. Rev. B **53**, 15 485 (1996); B. Anczykowski, D. Krüger, K.L. Babcock, and H. Fuchs, Ultramicroscopy **66**, 251 (1996); N.A. Burnham, O.P. Behrend, F. Oulevey, G. Gremaud, P.-J. Gallo, D. Gourdon, E. Dupas, A.J. Kulik, H.M. Pollock, and G.A.D. Briggs, Nanotechnology **8**, 67 (1997); O.P. Behrend, F. Oulevey, D. Gourdon, E. Dupas, A.J. Kulik, G. Gremaud, and N.A. Burnham, Appl. Phys. A: Mater. Sci. Process. **66**, S219 (1998).

[14] F.J. Giessibl, Phys. Rev. B **56**, 16 010 (1997); N. Sasaki and M. Tsukada, Jpn. J. Appl. Phys., Part 1 **37**, L533 (1998); H. Hölscher, W. Allers, U.D. Schwarz, A. Schwarz, and R. Wiesendanger, Phys. Rev. Lett. **83**, 4780 (1999); N. Sasaki and M. Tsukada, Jpn. J. Appl. Phys., Part 1 **39**, L1334 (2000); M. Gauthier, N. Sasaki, and M. Tsukada, Phys. Rev. B **64**, 085409 (2001); A. San Paulo and R. García, *ibid.* **64**, 193411 (2001).

[15] L. Nony, R. Boisgard, and J.-P. Aimé, Eur. Phys. J. B **24**, 221 (2001).

[16] A. Kühle, A.H. Sørensen, J.B. Zandbergen, and J. Bohr, Appl. Phys. A: Mater. Sci. Process. **66**, S329 (1998).

[17] J.P. Hunt and D. Sarid, Appl. Phys. Lett. **72**, 2969 (1998); N. Sasaki, M. Tsukada, R. Tamura, K. Abe, and N. Sato, Appl. Phys. A: Mater. Sci. Process. **66**, S287 (1998); W. Van der Water and J. Molenaar, Nanotechnology **11**, 192 (2000).

[18] S.I. Lee, S.W. Howell, A. Raman, and R. Reifenberger, Phys. Rev. B **66**, 115409 (2002).

[19] E. Doedel, A.R. Champneys, T.F. Fairgrieve, Y.A. Kuznetsov, B. Sandstede, and X. Wang, *AUTO97: Continuation and Bifurcation Software for Ordinary Differential Equations (with HomCont)* (Concordia University, Montreal, 1997).

[20] A.H. Nayfeh and D.T. Mook, *Nonlinear Oscillations* (Wiley, New York, 1979).

[21] J. Guckenheimer and P.J. Holmes, *Nonlinear Oscillations, Dynamical Systems, and Bifurcations of Vector Fields* (Springer, New York, 1983); S. Wiggins, *Introduction to Applied Nonlinear Dynamical Systems and Chaos* (Springer, New York, 1990).

[22] K. Yagasaki, SIAM (Soc. Ind. Appl. Math.) J. Appl. Math. **56**, 1720 (1996).

[23] K. Yagasaki, Nonlinear Dyn. **9**, 391 (1996).

[24] B.V. Derjaguin, V.M. Muller, and Y.P. Toporov, J. Colloid Interface Sci. **53**, 314 (1975).

[25] K. Yagasaki, "Bifurcations and chaos in tapping mode atomic force microscopy" (unpublished).

[26] S. Wolfram, *The Mathematica Book*, 5th ed. (Wolfram Media, Champaign, IL, 2003).

[27] The condition $d\Omega^h/dh>0$ is equivalent to $d\Omega^h/dI>0$ since $dI/dh=1/\Omega^h>0$, where I is the action of the periodic orbit $(\bar{\xi}^h(t), \bar{\eta}^h(t))$ in the planar Hamiltonian system (20). We also note that a resonant periodic orbit detected by the subharmonic Melnikov method is stable if $(dM^h/dt_0)(t_0)>0$ and it is unstable if $(dM^h/dt_0)(t_0)<0$ since $d\Omega^h/dh>0$ and $L^h(t_0)<0$ (see Theorem 3.2 of Ref. 22).

[28] K. Yagasaki, Discrete Contin. Dyn. Syst., Ser. B **3**, 423 (2003).